



# Hydrodeoxygenation of solvolysed lignocellulosic biomass by unsupported MoS<sub>2</sub>, MoO<sub>2</sub>, Mo<sub>2</sub>C and WS<sub>2</sub> catalysts

M. Grilc<sup>a</sup>, G. Veryasov<sup>b</sup>, B. Likozar<sup>a,c,\*</sup>, A. Jesih<sup>b,d</sup>, J. Levec<sup>a,c</sup>

<sup>a</sup> Laboratory of Catalysis and Chemical Reaction Engineering, National Institute of Chemistry, Hajdrihova 19, 1000 Ljubljana, Slovenia

<sup>b</sup> Department of Inorganic Chemistry and Technology, Jožef Stefan Institute, Jamova 39, 1000 Ljubljana, Slovenia

<sup>c</sup> Faculty of Chemistry and Chemical Technology, University Ljubljana, Aškerčeva 5, 1000 Ljubljana, Slovenia

<sup>d</sup> Center of Excellence in Nanoscience and Nanotechnology, Jamova Cesta 39, 1000 Ljubljana, Slovenia

## ARTICLE INFO

### Article history:

Received 25 June 2014

Received in revised form 11 August 2014

Accepted 19 August 2014

Available online 26 August 2014

### Keywords:

Fullerene-like MoS<sub>2</sub>

Liquefied biomass

Hydrotreatment

Decarbonylation/decarboxylation

Lumped deoxygenation model

## ABSTRACT

Hydrotreatment of liquefied lignocellulosic biomass was investigated at 300 °C under the total pressure of 8 MPa in a slurry reactor over unsupported molybdenum (disulphide, dioxide and carbide) and tungsten (disulphide) catalysts. Novel nanostructured urchin-like MoS<sub>2</sub> and inorganic-fullerene MoS<sub>2</sub> interconnected with carbon materials were synthesized and tested, while the influence of metal variation and the sulphide replacement with carbide or oxide was also investigated by using commercially available MoS<sub>2</sub>, Mo<sub>2</sub>C, MoO<sub>2</sub> and WS<sub>2</sub>. Catalysts were structurally characterised by field-emission scanning (SEM) and high-resolution transmission (HRTEM) electron microscopies, energy-dispersive X-ray (EDX) and Raman spectroscopies, as well as X-ray diffraction (XRD). The hydrodeoxygenation (HDO), decarbonylation, decarboxylation and hydrocracking kinetics of depolymerised cellulose, hemicellulose and lignin were determined according to the transformation of their functional groups in liquid phase, and the corresponding gaseous products by an innovative lumped kinetic model based on Fourier transform infrared spectroscopy. Unsupported MoS<sub>2</sub> catalysts showed high hydrogenolysis selectivity, the morphology clearly affecting its rate. A high HDO activity reflected in the mass balance and phase distribution of the upgraded liquid product by reducing tar residue and increasing the yield of oil phase with the gross calorific value of 38 MJ kg<sup>-1</sup> and oxygen content below 8.5 wt%.

© 2014 Elsevier B.V. All rights reserved.

## 1. Introduction

Utilisation of biomass as a renewable energy source has nowadays gained a great interest in petroleum-importing countries. Biomass is the most attractive sustainable carbon source, and less than 2% of the energy from natural biomass replacement is currently being used [1]. Waste lignocellulosic materials are an especially desirable feedstock, as they are abundant and their origin does not compete with food crops as in the case of the edible oils in biodiesel production or corn for bioethanol. However, solid lignocellulosic biomass is impractical to transport and store due to its low bulk density, and consequently a low volumetric energy density. To widen its applicability as a fuel, it is particularly desirable to convert it into a liquid product.

Lignocellulosic biomass liquefaction by the solvolysis in cheap renewable solvents such as glycerol, a by-product from biodiesel production, is a promising thermochemical biomass-to-liquid (BtL) conversion route, since it can be performed at significantly lower temperatures in comparison to other thermochemical technologies (e.g. pyrolysis or gasification). Process temperatures, as low as 170 °C, prevent extensive char and gas formation, and consequently lead to a higher liquid product yield and a higher gross calorific value (GCV) of the liquid product in comparison to pyrolysis. Solvolysed lignocellulosic biomass was successfully tested as a fuel in a gas turbine [2], but due to its high viscosity and a high content of chemically bonded oxygen (mass fraction over 40%), it is unsuitable for use as a transportation fuel without preceding upgrade.

Various biomass-derived oils, containing oxygenates such as alcohols, aldehydes, esters and carboxylic acids, can be upgraded to hydrocarbon fuels in the catalytic hydrotreatment process under a high-pressure hydrogen and in the presence of heterogeneous catalysts [3–5]. Beside the hydroprocessing of real bio-oils, chemical mechanisms were intensively studied on model compounds that represent depolymerized cellulose [6,7] and lignin [8,9] components, or simply oxygenates with various types and combinations

\* Corresponding author at: Laboratory of Catalysis and Chemical Reaction Engineering, National Institute of Chemistry, Hajdrihova 19, 1000 Ljubljana, Slovenia. Tel.: +386 1 4760283; fax: +386 1 4760300.

E-mail address: [blaz.likozar@ki.si](mailto:blaz.likozar@ki.si) (B. Likozar).

of functional groups [10,11]. Sulphided bifunctional catalysts such as NiMo/ $\gamma$ -Al<sub>2</sub>O<sub>3</sub> and CoMo/ $\gamma$ -Al<sub>2</sub>O<sub>3</sub> are traditionally used for hydrotreatment, where molybdenum is the active element, and the sulphur vacancies, located at the edges of MoS<sub>2</sub> nanoclusters, are the active sites responsible for hydrodeoxygenation (HDO), while nickel or cobalt serves as a promoter [11,12].  $\gamma$ -Al<sub>2</sub>O<sub>3</sub> support has been widely used because of its high surface area and acidic character, but on the other hand, it is unsuitable for HDO, as it is converted to boehmite (AlO(OH)) in the presence of water at elevated temperatures [5,13–15]. Al<sub>2</sub>O<sub>3</sub> support also showed high tendency for coke deposition caused by polymerisation reactions of unstable species on the catalyst surface [16], so the use of neutral (e.g. carbon) supports or the use of unsupported catalysts with either high surface area or sufficient activity seems promising. The use of unsupported MoS<sub>2</sub> is advantageous because of its low price and high selectivity towards HDO [17], while some forms of its diverse morphology might result in a high catalytic activity [18].

The most frequently applied route for the preparation of unsupported MoS<sub>2</sub> catalysts is the decomposition of ammonium thiomolybdates [19–24]. Intensive work was done on the investigations of the preparation conditions contribution to the catalytic activity of the resulting material [19]; by the thermal decomposition of (NH<sub>4</sub>)<sub>2</sub>MoS<sub>4</sub> (ammonium tetrathiomolybdate, ATTM), authors managed to obtain molybdenum sulphides with the specific surface areas of up to 88 m<sup>2</sup> g<sup>-1</sup>, while the hydrothermal decomposition of ATTM in the presence of an organic solvent was reported to give an amorphous MoS<sub>2</sub> with the surface area up to 368 m<sup>2</sup> g<sup>-1</sup> [18,23,24].

In this work, the ammonium thiomolybdates replacement with molybdenum halides or coordination precursors was introduced; specifically, the fine powders of MoI<sub>3</sub> or CpMoCl<sub>4</sub> were used for the preparation of molybdenum disulphide with morphology that was not reported up to date. Molybdenum halides are readily transformed into sulphides at the elevated temperature in the reductive atmosphere of H<sub>2</sub>/H<sub>2</sub>S/Ar gas mixture. In previous work, the urchin-like MoS<sub>2</sub> units formation from MoI<sub>3</sub> precursor was only briefly communicated [25], while this work provides detailed insights into its catalytic activity. In this work, the formation of first MoS<sub>2</sub> inorganic fullerenes, with ~12 nm unit size, interconnected by carbon (MoS<sub>2</sub>(IF)/C) is reported from CpMoCl<sub>4</sub> precursor. Inorganic fullerenes (IF) are expected to possess a high concentration of surface active sites [26], while the role of carbon is to affix MoS<sub>2</sub>(IF) units, preserving the original shape of agglomerates; however, it can also reduce the catalytic activity by blocking the active sites on the IF surface.

The activity and selectivity comparison for various prepared and commercially available unsupported Mo catalysts in oxide, carbide and sulphide form, and commercial WS<sub>2</sub> nanotubes is based on the apparent kinetic rate constants for hydrodeoxygenation, decarboxylation, decarbonylation and hydrocracking of solvolytic oil. Kinetic model was developed and focused on the removal of the main oxygen-containing moieties in liquid phase, and the formation of corresponding gaseous products. The main emphasis of this work is to compare the influence of different morphologies of the unsupported MoS<sub>2</sub> on catalytic performance and to parallel the activity with commercially available NiMo/ $\gamma$ -Al<sub>2</sub>O<sub>3</sub> catalysts, reported in previous studies [27]. Molybdenum replacement with tungsten, as well as sulphide substitution with carbide or oxide, was also investigated by commercially available materials.

## 2. Experimental

### 2.1. Solvolysis oil

Solvolyzed biomass was provided by a company that runs the pilot plant for the liquefaction of the lignocellulosic biomass waste

in acidified glycols, strictly following the procedure from the literature [2,28]. The mass fraction of the dry sawdust in the solvolysis oil was 25%, the rest being glycerol and diethylene glycol mixture (1:1 by mass), containing 3 wt% of *p*-toluenesulphonic acid. The liquefied biomass had the gross calorific value (GCV) of 21.9 MJ kg<sup>-1</sup> and the oxygen mass fraction of 43.3%, including the dissolved water (less than 20 g kg<sup>-1</sup>). The detailed characterization of the liquefied biomass can be found in our previous study [29], or elsewhere in the literature [2].

### 2.2. Catalyst preparation and characterisation

MoS<sub>2</sub>(IF)/C catalyst was synthesized by the sulphidisation of CpMoCl<sub>4</sub> (Sigma–Aldrich, 95 wt%), where Cp represents cyclopentadiene, in the quartz boat inside quartz tube. To prevent the decomposition of material, caused by the contact with moisture or oxygen, it was kept under the argon atmosphere in dry-box, while a glass vessel was used for boat transfer. 850 mg of CpMoCl<sub>4</sub> was placed into the boat (75 × 16 × 12 mm) and carefully transferred to quartz tube (970 mm length; 22 mm diameter). Quartz tube was purged for 30 min with the constant flow of the sulphidising gas mixture (60 mL min<sup>-1</sup>; 2/2/96 vol% of H<sub>2</sub>/H<sub>2</sub>S/Ar; Air Liquide) before a sample was heated to 800 °C with the heat-up rate of 2000 °C h<sup>-1</sup>. It was then kept at the set temperature for 3 h under the constant flow of sulphidising agent, and subsequently left to cool down to the ambient temperature.

Urchin-like MoS<sub>2</sub> was prepared through the sulphidisation of MoI<sub>3</sub> that was synthesised from Mo(CO)<sub>6</sub> (Sigma–Aldrich, 98 wt%) and I<sub>2</sub> (Sigma–Aldrich, 99.99 wt%), following the procedure, reported in our previous work [25]. Bulk MoO<sub>3</sub> (Sigma–Aldrich, 99 wt%), MoS<sub>2</sub> (Sigma–Aldrich, 99 wt%) and WS<sub>2</sub> nanotubes (NanoMaterials, 99 wt%) were used as-received without further purification.

Raman spectra of crystals were measured with Horiba Jobin–Yvon LabRAM HR spectrometer using the 632.81 nm excitation line of the He–Ne laser with the power of 17 mW. To prevent the decomposition of a sample, density filter was applied to reduce the power of the laser to 1.7 mW. An Olympus ×50 long-distance objective was used. Spectra were obtained by accumulating 20 scans with the integration time of 5 s. Spectrometer was calibrated using Si polycrystalline plate as the standard with the characteristic band at 520.6 cm<sup>-1</sup>. Field emission scanning electron microscopy (FE-SEM; Jeol 7600) and high-resolution transmission electron microscopy (HRTEM; Jeol JEM-2100) was used for the characterisation of the morphology and structure of samples, while energy-dispersive X-ray spectroscopy (EDX) analysis was applied to evaluate the carbon distribution over the MoS<sub>2</sub>(IF)/C. For elemental analysis, Elemental MICRO cube elemental analyser was used, whereas BET analysis was performed using Micrometrics Gemini IV apparatus with the N<sub>2</sub> gas at -196 °C. X-ray powder diffraction data were collected using XRD equipment (Rigaku, AFC7, Cu K $\alpha$ 1 and Cu K $\alpha$ 2 radiation with 40 kV and 20 mA) over the 2 $\theta$  range of 10–75°, with the step size of 0.05°, and the counting time of 5 s per step.

### 2.3. Hydrotreatment reactions

Solvolyzed oil hydrotreatment experiments were performed in the cylindrical 300 mL batch stainless steel autoclave (Parker Autoclave Engineers) with the inner diameter of 43 mm and the height of 210 mm (Fig. SD.1). The reactor was equipped with magnetically driven Rushton turbine impeller with the diameter of 30 mm that was located 25 mm above reactor bottom. The reactor was filled with 125 mL of cold reaction mixture containing homogenised solvolytic oil and tetralin (Sigma–Aldrich, ≥97 wt%) in a 3:1 mass ratio. The mass fraction of the catalyst in the reaction mixture for

all catalytic experiments was 1.5% with respect to solvolysis oil. The reactor was sealed, closed and purged with hydrogen (Messer, 5.0) by pressurization–depressurization cycles at 1 and 2 MPa to evacuate the air from its headspace. Hydrogen pressure was elevated up to 8 MPa, the continuous purge ( $1.0 \text{ L}_N \text{ min}^{-1}$ ) through the reactor with fresh hydrogen was established, and reaction mixture was consequently subjected to intensive stirring with the agitation speed of  $1000 \text{ min}^{-1}$  to ensure a high hydrogen availability in liquid phase and on catalyst surface. Previous study showed the absence of the external mass-transfer limitations at similar reaction conditions [29], while intra-particle mass-transfer resistance was neglected because of the use of the catalyst in powder form. The experiment was started at the room temperature; consequently, reaction temperature was elevated by the heat-up rate of  $7.5 \text{ K min}^{-1}$  to  $300^\circ\text{C}$  by using electric jacket heater, controlled with PID regulator (SR25, Shimaden). After 60 min at  $300^\circ\text{C}$ , the reactor was rapidly cooled down by dipping the reactor vessel into icy water, while subsequently, pressure was gradually decreased and the reactor was purged with nitrogen before opening.

#### 2.4. Gas, liquid and solid phase analysis

The cooled and decompressed gas from the reactor was analysed online by Fourier transform infrared (FTIR) spectroscopy (Spectrum 100, Perkin Elmer), where CO, CO<sub>2</sub>, methane and propane contents were quantified. Six liquid samples were collected during each run, applied on the silicon wafer by a thin-film applicator and analysed by FTIR. Each sample was applied and scanned seven times in the range of  $450\text{--}4000 \text{ cm}^{-1}$  to calculate the average measured value. The quantification of the components in gas phase and the moieties in liquid phase was performed by following the methodology, developed in our previous study [27]. After reactor opening, reaction mixture was centrifuged at  $7500 \text{ min}^{-1}$  for 10 min to separate liquid phases and to sediment the catalyst. The elemental composition of the separated phases was determined by CHNS(O); samples were packed into aluminium envelopes and flushed with He prior to analyses.

The gross calorific value (GCV) of each phase was calculated by using the Dulong formula, in which C, H, O and S are the mass fractions of carbon, hydrogen, oxygen and sulphur. The formula,  $\text{GCV} = 35.5\text{C} + 114.8\text{H} + 9.5\text{S} - 14.5\text{O}$ , gives GCV in  $\text{MJ kg}^{-1}$ .

Catalyst was separated from the tar phase by filtration, after the latter was diluted in tetrahydrofuran. After the multiple rinses with ethanol or tetrahydrofuran, and the subsequent drying in the N<sub>2</sub> atmosphere at the room temperature, the mass of the collected catalyst was determined before its characterisation.

#### 2.5. Hydrotreatment model

Reaction pathways (Fig. 1) for the catalytic hydrotreatment of biomass-derived oils was adopted from our previous work [27] and is based on the transformation of the oxygen-containing functional groups, namely hydroxyl and carbonyl group, determined in the liquid phase by FTIR, and the related gaseous products. It allows following the reactions of hydrodeoxygenation, dehydrogenation, decarbonylation, decarboxylation and hydrocracking.

Modelling was performed in Matlab 7.12.0. For optimization purposes, both simplex and non-linear least-squares approximation search methods were used to determine the kinetic parameters  $E_{an}$  and  $A_n$  for each reaction, where the parameters corresponded to the minimum of the objective function, given as Eq. (1):

$$f(Ea1, A1, Ea2, A2, \dots, Ean, An)$$

$$= \sum_{i=1}^I (y_i^{\text{meas}} - y_i^{\text{calc}}(Ea1, A1, Ea2, A2, \dots, Ean, An))^2 \quad (1)$$

$$y_i = \frac{C_i}{C_{OH}} \quad (t = 0) \quad (2)$$

Here  $i$  represents the index of a reaction or a corresponding lump ( $I$  is their number) and  $y_i$  is the relative concentration of the lump  $i$ .  $E_{an}$  represents the activation energy, and  $A_n$  the pre-exponential factor of reaction  $n$ . Superscripts meas and calc refer to the measured and calculated values. The values of the relative concentrations ( $y_i^{\text{calc}}$ , calculated by normalizing the concentration,  $C$ , to the initial OH group concentration  $C_{OH}(t=0)$ ) during reactions' time were determined by solving the set of differential mass balances, formulated according to reaction scheme (Fig. 1), involving seven lump components and six chemical reactions. Runge–Kutta algorithm was used to numerically solve the set of differential equations.

External mass-transfer resistance was neglected as it was eliminated by intensive stirring and the continuous purge of the fresh hydrogen through the reaction mixture at 8 MPa, while internal mass-transfer limitations were expected to be negligible as the catalysts in the powder form (Fig. SD.2) with a low porosity were used. Intrinsic rate constants are therefore very close to global kinetic rate constants ( $k_n$ ):

$$r_n = k_n y_i \quad (3)$$

The constant purge of the fresh hydrogen at 8 MPa assured the sufficient and permanent hydrogen availability for the hydrotreatment of reaction mixture and on catalysts' surface. The influence of hydrogen pressure was not investigated in this study, but the concentration of dissolved hydrogen may be considered to be included in the corresponding rate constants. The orders of hydrocracking rates ( $n=5, 6$ ) were set to zero, in accordance to our experimental observations in present and previous work [27,29].

$$r_n = k_n \quad (4)$$

Apparent rate constants were considered as temperature-dependent according to the Arrhenius equation ( $R$  is the gas constant) during the heating-up part of experiments (until the temperature of plateau was reached), while rate constants were calculated at  $300^\circ\text{C}$  for the isothermal segment of experiments, alongside with their 95% confidence intervals.

$$k_n(T(t)) = A_n \exp\left(-\frac{E_{an}}{RT(t)}\right) \quad (5)$$

Balances and initial values were used analogously as for the model in our previous work [27].

### 3. Results and discussion

#### 3.1. Catalyst characterisation

SEM images of all materials tested for catalytic activity are shown in Fig. SD.2; commercially available MoS<sub>2</sub> and Mo<sub>2</sub>C appear as agglomerates with the particle size above  $1 \mu\text{m}$ , while MoO<sub>2</sub> is a crystalline material with the particle size around  $500 \text{ nm}$ . Tungsten disulphide nanotubes have the tube lengths of a few micrometres and the average tube diameter of about  $200 \text{ nm}$ . Particle sizes estimated on the basis of SEM images (Fig. SD.2) and the results of BET measurements are collected in Table 1.

Synthesized samples had a significantly higher surface area compared to commercial MoS<sub>2</sub> powder. Urchin-like material (Fig. 2) was found to have the specific surface area of  $26 \text{ m}^2 \text{ g}^{-1}$ , while MoS<sub>2</sub>(IF)/C sample exhibited the highest specific surface area of  $303 \text{ m}^2 \text{ g}^{-1}$ , since it was prepared from CpMoCl<sub>4</sub> and contained carbon, resulting from reductive ligands decomposition reaction. Total CHNS analysis gave the elemental composition of 21.2 wt% C

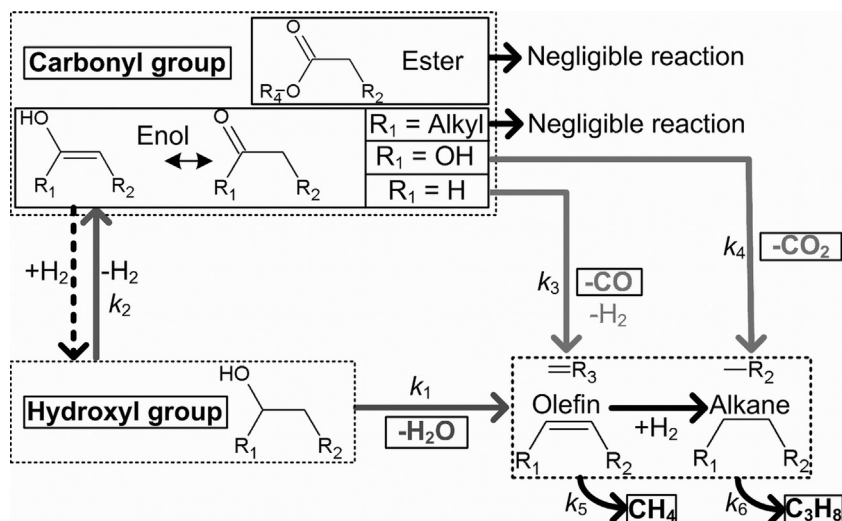


Fig. 1. Proposed reaction mechanism for hydrodeoxygenation, decarbonylation, decarboxylation and hydrocracking over examined heterogeneous catalysts.

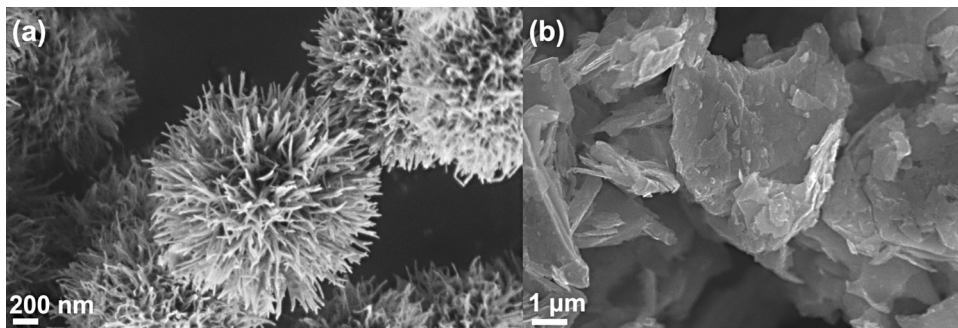


Fig. 2. Scanning electron microscopy (SEM) image of (a) urchin-like MoS<sub>2</sub> and (b) commercially available MoS<sub>2</sub>.

and 30.3 wt% S, the latter mirroring the material Mo:S:C molar ratio of 1.0:1.9:3.5. Stoichiometric ratio indicates that Mo was successfully sulphided, while present carbon is not covalently bonded with Mo. Carbon is formed as amorphous phase as there were no diffraction peaks, corresponding to an ordered carbon phase, observed in XRD diffractograms. The formation of carbon containing materials with the Mo:S:C mole ratio of 1:(2-X):Z, was also observed for the sulphidation of (NR<sub>4</sub>)<sub>2</sub>MoS<sub>4</sub> salts (X was minute), where R represents an C5–C8 alkyl group [30]; it was noted that surface area appears significantly more developed in the carbon-containing materials in comparison to neat molybdenum disulphide.

According to the Raman spectra (Fig. 3) of MoS<sub>2</sub>(IF)/C, carbon phase is actually present as charcoal [31]. The Raman spectra of commercial and urchin-like sample were briefly reported in previous work [25] and are added for comparative purposes. The Raman frequencies in the spectrum of MoS<sub>2</sub>(IF)/C are in good agreement with those pertinent to the spectra of MoS<sub>2</sub> fullerenes reported by Frey *et al.* [32].

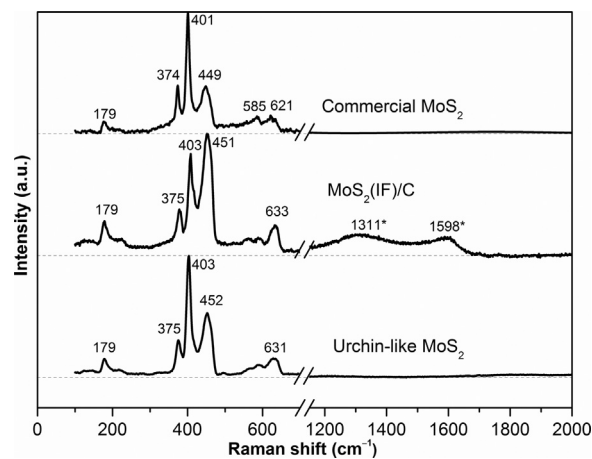


Fig. 3. Raman spectra of commercial MoS<sub>2</sub>, MoS<sub>2</sub>(IF)/C and urchin-like MoS<sub>2</sub> catalysts; bands marked with \* are attributed to carbon.

Table 1  
Characteristics of catalysts used for hydrotreatment tests.

Sample	Particle size (μm)	Specific surface area (m <sup>2</sup> g <sup>-1</sup> )	Pore size (Å)	Pore volume (cm <sup>3</sup> g <sup>-1</sup> )
Urchin-like MoS <sub>2</sub>	1	26	270	0.1737
MoS <sub>2</sub> (IF)/C	50–100	303	19	0.1463
Commercial MoS <sub>2</sub>	3–7	5	217	0.0261
MoO <sub>3</sub>	0.2–1.0	5	137	0.0170
Mo <sub>2</sub> C	1–5	3	118	0.0085
WS <sub>2</sub> nanotubes	0.1–0.3 <sup>a</sup>	6	193	0.0275

<sup>a</sup> Nanotube diameter.



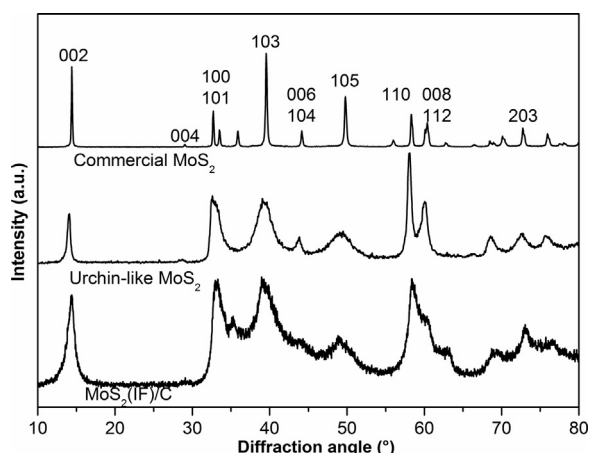


Fig. 4. XRD of commercial MoS<sub>2</sub>, urchin-like MoS<sub>2</sub> and MoS<sub>2</sub>(IF)/C catalysts.

XRD patterns of commercial MoS<sub>2</sub>, urchin-like MoS<sub>2</sub> and MoS<sub>2</sub>(IF)/C are given in Fig. 4. The broadening of peaks is caused by a smaller crystallite size in the synthesized materials, indicating that MoS<sub>2</sub>(IF)/C sample has a lower crystal domain size (8 nm), compared to urchin-like material (18 nm), or commercial MoS<sub>2</sub> (55 nm) [25], according to Scherrer equation [33]. Judging by the TEM image of MoS<sub>2</sub>(IF)/C, presented in Fig. 5a, MoS<sub>2</sub> nanoparticles appeared in the fullerene-like form with the unit size of about 12 nm, which is slightly higher than the calculated value, given by the Scherrer equation; the figure also reveals the carbon inclusions in between MoS<sub>2</sub> clusters. To the best of our knowledge, this is the first example of the MoS<sub>2</sub>(IF)/C composite formation in a single-step synthesis.

The carbon removal process from MoS<sub>2</sub>(IF)/C was investigated, since it might lead to enhanced catalytic activity of the material. According to EDX mapping analysis (Fig. 6a, c and e), carbon was evenly distributed over the sample before carbon removal. Two approaches were examined; specifically, the prolonged heating in the H<sub>2</sub>/H<sub>2</sub>S/Ar gas mixture at elevated temperatures, and oxidation, followed by sulphidisation.

The heating at 800 °C in H<sub>2</sub>/H<sub>2</sub>S/Ar gas mixture reduced the carbon content to 20 wt%, while heating the sample at 1000 °C resulted in the carbon removal to 7 wt% and the sample with the specific surface area of 204 m<sup>2</sup> g<sup>−1</sup> was obtained, where the morphology of material retained unchanged. Applying the second technique, the sample was oxidised at 400 °C in O<sub>2</sub>/Ar gas mixture (30/70 vol%, 60 mL min<sup>−1</sup>) for 4 h and sulphidised afterwards for 3 h at 400 °C (2/2/96 vol% H<sub>2</sub>/H<sub>2</sub>S/Ar, 60 mL min<sup>−1</sup>). Carbon-free material with the surface area of only 20 m<sup>2</sup> g<sup>−1</sup> was formed within the first stage, while the subsequent sulphidisation of the resulting MoO<sub>3</sub> renders a thin plate-layered MoS<sub>2</sub> structure formation (Fig. 6b, d and f).

Both mentioned processes induced a significant decrease in specific surface area; however, the original agglomerated structure was retained after the treatment with H<sub>2</sub>/H<sub>2</sub>S/Ar gas mixture. Oxidation, followed by sulphidisation, caused the complete change of the physical appearance of the material (Fig. 6b, d and f). Presumably, the decomposition of CpMoCl<sub>4</sub> in the presence of a sulphidising agent introduces the evolution of CpMoSCL<sub>2</sub> and CpMoS<sub>2</sub> as intermediate moieties; analogous products, CpMoO<sub>2</sub> and CpMoOCl<sub>2</sub>, are known to form from CpMoCl<sub>4</sub> in the presence of moisture [34], and the formation of carbon phase occurs due to degradation of cyclopentadiene, strongly bonded to molybdenum core.

### 3.2. Hydrotreatment products

Fig. 7 shows the mass balance and oxygen content in the liquid fractions for all hydrotreatment runs. The liquid fraction from reactor vessel was homogeneous, while the centrifugation at a high revolution rate in most cases resulted in the separation of three phases, namely the oil phase (non-polar) appeared on the top, the yellow polar (aqueous) phase in the middle, and the viscous fraction containing the unreacted or partly polymerised liquefied biomass on the bottom.

Hydrolysed and depolymerised products from cellulose and hemicellulose, such as levulinic acid and hydroxymethylfurfural, were gradually hydrodeoxygenated during the hydrotreatment in numerous consecutive steps, and form the polar components (polar phase) in the initial HDO stages, before they are finally transformed into the non-polar compounds, soluble in the oil phase. Depolymerised lignin compounds, such as guaiacol and coniferyl alcohol, initially possess a much lower content of chemically-bonded oxygen and have a lower polarity, so they might readily transfer into the oil phase already within the initial stages of HDO. On the other hand, phenols and di-phenyl ethers are known to be much more resistant to HDO in comparison to alkyl alcohols; consequently, the compounds originating from lignin may have been responsible for the incomplete deoxygenation of the final product [5]. The goal of HDO is a high conversion of liquefied biomass and a high yield of the oil phase with as low oxygen content as possible. Fig. 7 reveals that the use of all unsupported MoS<sub>2</sub> catalysts resulted in the phase separation of liquid products; specifically, oil phase yield is the highest for urchin-like MoS<sub>2</sub> confirming its anticipated high HDO activity, while the lowest presence of tar phase indicates a high conversion of liquefied biomass and the inhibition of polymerisation reactions. The yield of the polar (aqueous) phase is also the highest for urchin-like MoS<sub>2</sub>. For the latter material, the polar phase was transparent, of a low viscosity, whereas its elemental composition predicted the calorific value of 11.5 MJ kg<sup>−1</sup>. The oxygen content for both oil and polar phases was very similar for all runs using MoS<sub>2</sub> catalysts, which pertained to their physical appearance as well.

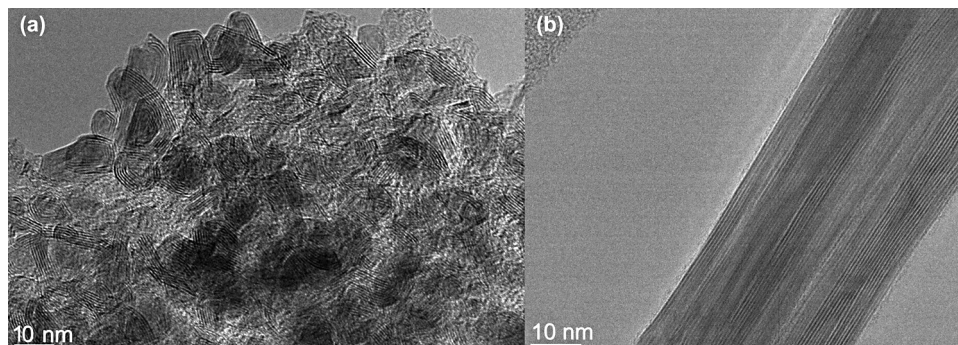


Fig. 5. TEM image of MoS<sub>2</sub>(IF)/C (a) and radial branch of urchin-like MoS<sub>2</sub> (b).

Hydrotreatment over unsupported commercial  $\text{MoO}_2$  resulted in similar product yields as for commercial  $\text{MoS}_2$ . It should be noted that the polar phase could not be separated from the tar phase for the experiments with  $\text{Mo}_2\text{C}$ ,  $\text{WS}_2$  and for the blank run, as liquid products had a significantly higher viscosity in comparison to liquid products, obtained by using  $\text{MoO}_2$  or  $\text{MoS}_2$  in any form. The yield of joint polar and tar phase was the highest for those runs; consequently, oil phase yields were among the lowest.  $\text{WS}_2$  nanotubes caused a very specific behaviour of reaction system; as the yield of oil phase was among the lowest, a significant amount of light, condensed fraction was collected from the water-cooled condenser with the GCV of  $39 \text{ MJ kg}^{-1}$ . Its FTIR analysis confirmed the presence of alkyl and carbonyl groups, while C–O or O–H groups were not present at all. It is expected that the light fraction comprised very volatile (but condensable) severely deoxygenated components, which still contained ketone or aldehyde groups that are obviously very resistant at the applied (rather mild) HDO conditions. In overall,  $\text{WS}_2$  nanotubes are not a suitable material for solvolysed biomass HDO due to poor rheological properties of the resulting product and a low yield of the separated oil phase and condensed fraction.

The FTIR spectra of the gas phase during the hydrotreatment over urchin-like  $\text{MoS}_2$  are presented as a function of reaction time

in Fig. 8, while for the reaction with  $\text{MoS}_2(\text{IF})/\text{C}$  and blank run, 3D FTIR spectra are presented in Fig. SD.3. The formation of  $\text{CO}_2$ ,  $\text{CO}$ ,  $\text{CH}_4$  and  $\text{C}_3\text{H}_8$  was detected by FTIR at characteristic wavenumbers presented in Table SD.1, and these components were quantified following the procedure from the previous work [27]. In comparison to the hydrotreatment results for  $\text{NiMo}/\gamma\text{-Al}_2\text{O}_3$  catalyst [27], it can be concluded that all characteristic bands are matching, while the appearance of the new bands in the range of  $2700\text{--}2850 \text{ cm}^{-1}$  and simultaneously at  $1720\text{--}1780 \text{ cm}^{-1}$  reveal the presence of the light aldehydes in gas phase (not present for  $\text{NiMo}/\gamma\text{-Al}_2\text{O}_3$ ,  $\text{Pd}/\gamma\text{-Al}_2\text{O}_3$  or  $\text{Ni}/\text{SiO}_2\text{-Al}_2\text{O}_3$ ). Their formation can be attributed to the thermal deformylation without catalytic decarbonylation due to a low acidity of the unsupported catalysts (in comparison to silica- or alumina-supported catalysts), resulting in a low promotion of C–C bond cleavage, and therefore, a weakly catalysed decarbonylation. This can be confirmed by the results of non-catalysed run (Fig. SD.3), as the presence of the carbonyl group in the gas phase was similar.

The following sections will more meticulously detail that all unsupported catalysts used in this study had relatively little effect on gas formation, as gas-phase compositions were very similar to the one for the non-catalysed run. The formation of gases, determined by FTIR, represented the mass fraction of approximately 5%

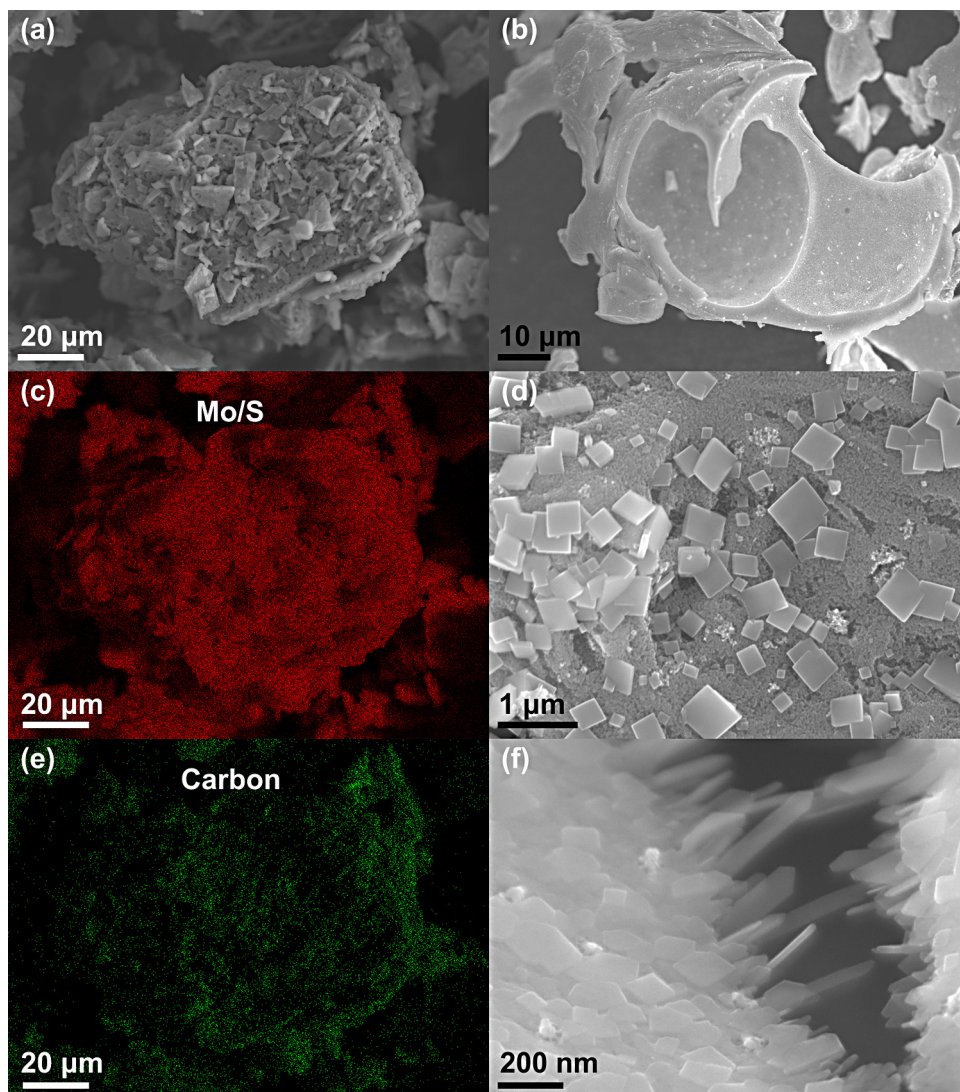


**Fig. 6.** Scanning electron microscopy (SEM) image of  $\text{MoS}_2(\text{If})/\text{C}$  prepared from  $\text{CpMoCl}_4$  (a) and its energy-dispersive X-ray spectroscopy mapping representing Mo and S distribution (c) and C distribution (e); product obtained after oxidation and re-sulphidization of prepared  $\text{MoS}_2(\text{If})/\text{C}$  (b) and its close-up view (d, f).

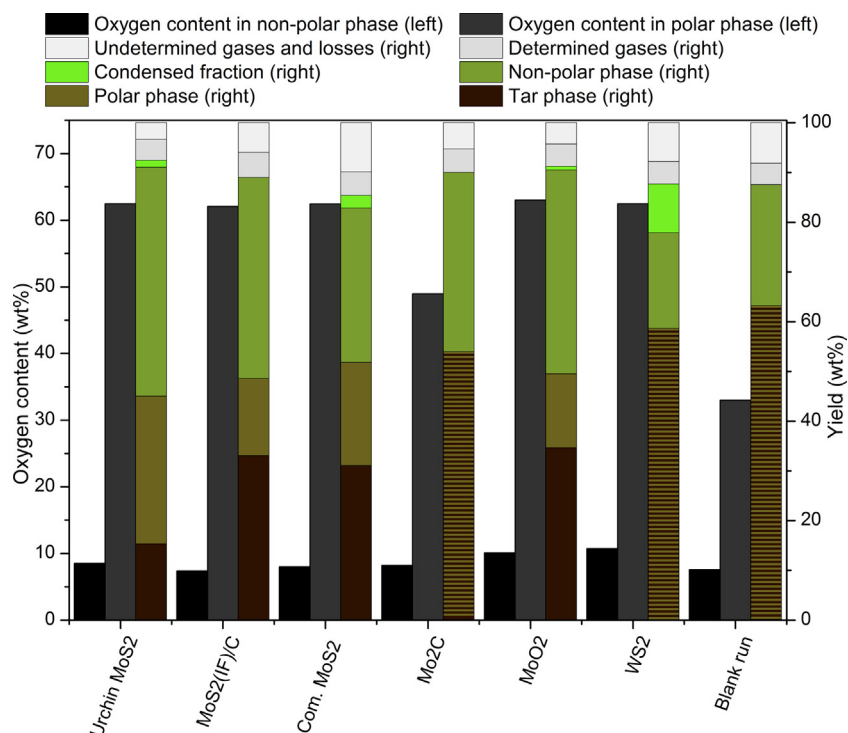


**Fig. 7.** Oxygen content in non-polar (oil) and polar phase and mass balances of reaction products using different catalysts for hydrotreatment of liquefied lignocellulosic biomass (300 °C; 8 MPa H<sub>2</sub>; 1 h).

for all runs, which indicates that the yield of gases is low and rather similar for all unsupported MoS<sub>2</sub>, MoO<sub>2</sub>, Mo<sub>2</sub>C or WS<sub>2</sub> catalysts. The gases that were not detected or quantified by FTIR were implicitly included in the losses of the mass balance in Fig. 7. The main cause of the latter was actually the viscous tar phase that hampered its removal from lining and stirrer. As mass balance closure was relatively high for all experiments (94 ± 3 wt%), it can be concluded that the mass of formed gases, that remain undetected by FTIR, was indeed low and was therefore neglected for modelling study.

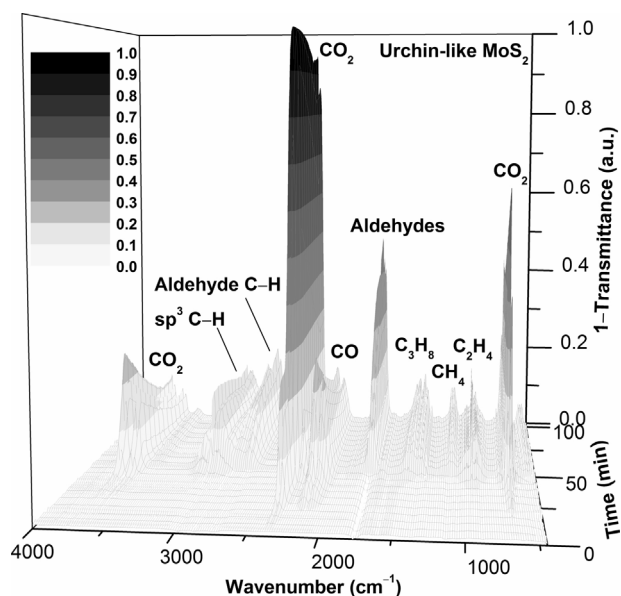
Although tar phase appeared semi-solid for the runs with Mo<sub>2</sub>C, WS<sub>2</sub> catalysts and without the latter, it was always easily dissolved

in tetrahydrofuran. No other solid products beside the catalyst were collected after filtration, while the mass of cleaned and dried spent catalyst generally corresponded to its initial (fresh) mass. Fig. SD.4 shows that the used MoS<sub>2</sub>(If)/C and urchin-like MoS<sub>2</sub> catalysts retained their shape and morphology and could therefore be reused. In the case of the decreased catalytic activity, caused by the reduction of sulphide content, either catalyst can simply be reactivated by sulphidisation, whereas reduction can also be prevented with the addition of sulphiding spike into reaction mixture.

### 3.3. Modelling results

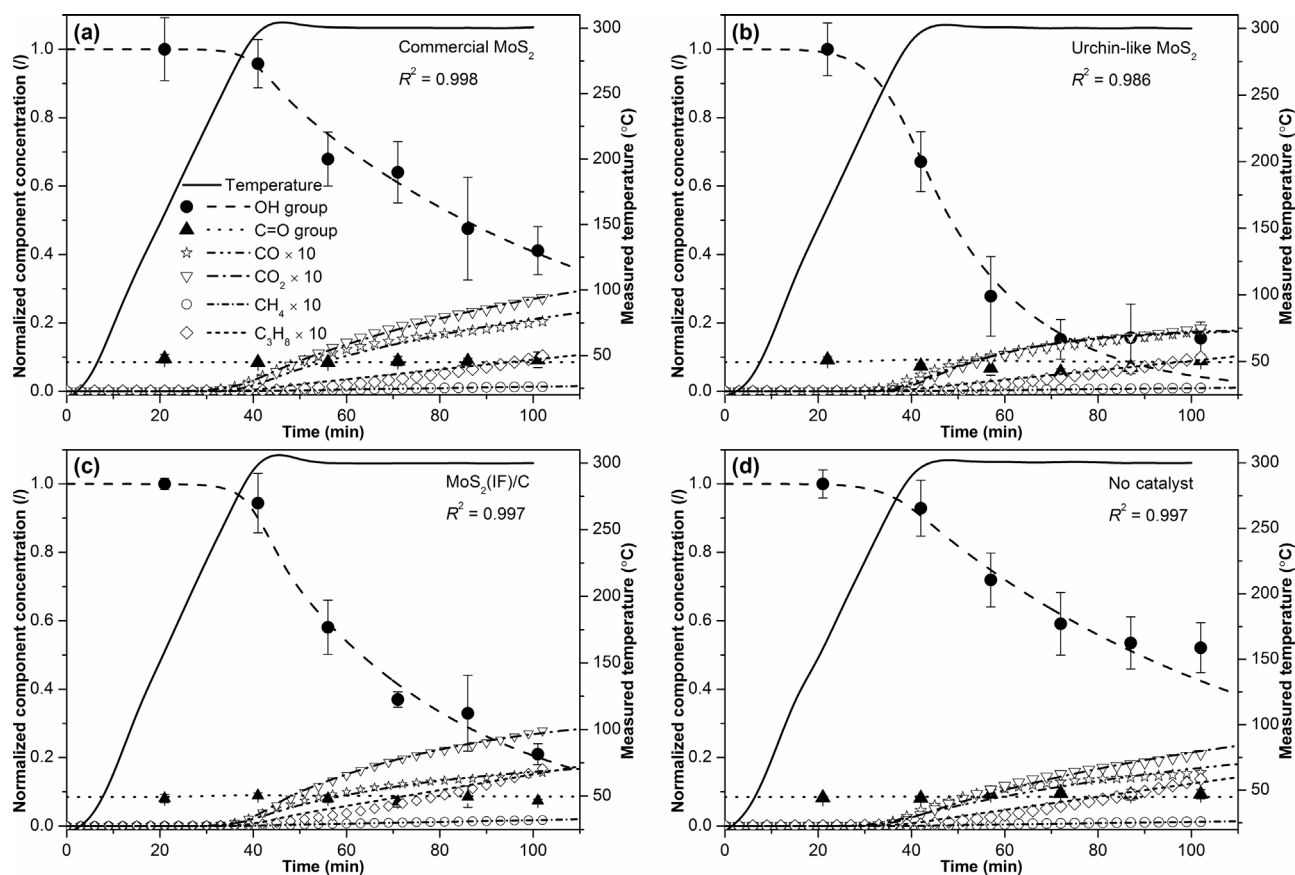
Apparent rate constants, collected in Table 2, were calculated for the isothermal part of the process at 300 °C from the parameters  $A_n$  and  $E_{an}$  (Eq. (15)) that correspond to the minimum of the objective function given by Eq. (1). Generally, the apparent rate constants at 300 °C are much more representative and reliable than  $A_n$  and  $E_{an}$  pair, as those were used to describe the non-isothermal part of reactions, which was short in our case, and therefore the calculated parameters  $A_n$  and  $E_{an}$  have a comparably lower parameter confidence for the general temperature dependence prediction of reaction rates. The apparent kinetic constants for the hydrotreatment over the commercially available sulphided NiMo/γ-Al<sub>2</sub>O<sub>3</sub> at 300 °C and 8 MPa of hydrogen pressure were added as a comparison.

Fig. 9 shows experimental and modelling results based on the FTIR measurements for different unsupported MoS<sub>2</sub> catalysts in comparison to blank run. It is evident that the highest rate of hydroxyl group removal was achieved by the urchin-like MoS<sub>2</sub> material, where the catalysed hydrogenolysis route was predominant as opposed to homogeneous decarbonylation and decarboxylation. According to the calculated apparent kinetic constants ( $k_1$ ) in Table 2, urchin-like MoS<sub>2</sub> exhibits a three-times higher hydrodeoxygenation activity in comparison to the commercially available MoS<sub>2</sub>, as nearly 85% hydroxyl group conversion is reached within 30 min at 300 °C. At that time, reaction obviously



**Fig. 8.** FTIR spectra of gas phase as a function of time for hydrotreatment process by using urchin-like MoS<sub>2</sub> catalyst.





**Fig. 9.** Experimental (symbols) and modelling (lines) results of hydrotreatment using unsupported MoS<sub>2</sub> catalysts or no catalyst; all experiments were performed at the same conditions: temperature of 300 °C, heat-up rate of 7.5 K min<sup>-1</sup>, total pressure of 8 MPa, stirring speed of 1000 min<sup>-1</sup>, 25 wt% of tetralin per mass of liquid phase and 1.5 wt% of catalyst per mass of liquefied biomass (except for blank run); values of normalized gas concentrations (CO<sub>2</sub>, CO, CH<sub>4</sub> and C<sub>3</sub>H<sub>8</sub>) have been multiplied by the factor of 10 to grant better clarity in given scale; legend refers to all subfigures.

reaches thermodynamic equilibrium, as both hydroxyl and carbonyl group concentrations generally remain unchanged for the further 30 min of reactions [25]. This hydroxyl group behaviour could not be described by the lumped kinetic model after 30 min, since it assumes the iso-reactivity of the reactive compounds within a lump, which can practically not be assured for such a complex feedstock. Residual hydroxyl groups might correspond to very resistant (poly)phenolic compounds that could not be deoxygenated at present reaction conditions, as they are reported to require up to 350 °C for successful HDO, according to the comparable reactivity scale of oxygenated groups reported by Elliott [5].

MoS<sub>2</sub>(IF)/C also exhibits a significantly higher HDO activity in comparison to commercially available MoS<sub>2</sub> or other unsupported catalysts (MoO<sub>3</sub>, Mo<sub>2</sub>C or WS<sub>2</sub>), presented in Fig. 10, and is comparable to that of the industrially applied NiMo/γ-Al<sub>2</sub>O<sub>3</sub> catalyst in sulphided form. The use of all unsupported MoS<sub>2</sub> materials led to very high selectivity of hydroxyl group HDO (between 93 and 97%) in comparison to decarbonylation and decarboxylation, which is advantageous in terms of a high yield of liquid product, as carbon is not removed from the feedstock during upgrade. Ruinart de Brimont *et al.* also reported a very selective HDO using the neat unsupported MoS<sub>2</sub>, where 98 mol% selectivity towards HDO was observed at 20% conversion [17]. The doping with nickel sulphide up to 0.43 Ni/Mo molar ratio increases overall deoxygenation rate, but severely sacrifices the HDO selectivity (only 36 mol%) in favour to decarbonylation/decarboxylation. If the results of the hydrotreatment over the sulphided commercially available NiMo/γ-Al<sub>2</sub>O<sub>3</sub> (Fig. 10) are compared with the ones obtained over

the unsupported MoS<sub>2</sub> (Fig. 9), a significantly higher decarboxylation rate can be observed, while the HDO selectivity of hydroxyl group remained above 96% as a result of the completely inhibited decarbonylation reaction.

Beside nickel sulphide absence, the lack of acid sites contributes to a low tendency for C–C bond cleavage as well; therefore, hydrocracking or decarbonylation/decarboxylation reactions were not significantly enhanced in the presence of MoS<sub>2</sub> catalysts. The calculated confidence intervals for decarbonylation and decarboxylation rate constants ( $k_3$  and  $k_4$ ) were relatively wide, since the precursors for decarbonylation and decarboxylation are being formed by the dehydrogenation of primary hydroxyl group ( $k_2$ ) that is a few orders of magnitude slower than consequent decarbonylation ( $k_3$ ) or decarboxylation ( $k_4$ ), and therefore represents the rate-determining step for CO and CO<sub>2</sub> formation. A low rate constant  $k_2$  in comparison to  $k_3$  and  $k_4$  also results in a rather minute concentration of intermediate (reactive carbonyl group), which is also in accordance with the observations from the literature [35]. Various pairs of  $k_3$  and  $k_4$  values led to a good agreement between the experimental and calculated values given that both constants were several orders of magnitude higher than  $k_2$ , yet their ratio ( $k_4/k_3$ ) remained unchanged. According to the reaction mechanism in Fig. 1, it can be concluded that  $k_2$  determines the rate of CO and CO<sub>2</sub> formation, while the ratio between  $k_3$  and  $k_4$  determines the selectivity between decarbonylation and decarboxylation.

The individual calculated values of  $k_3$  and  $k_4$  are therefore not expected to be very accurate and cannot be mutually compared for different experiments in a direct fashion in order to evaluate the proneness of materials to catalyse CO or CO<sub>2</sub> formation. Instead,  $k_2$



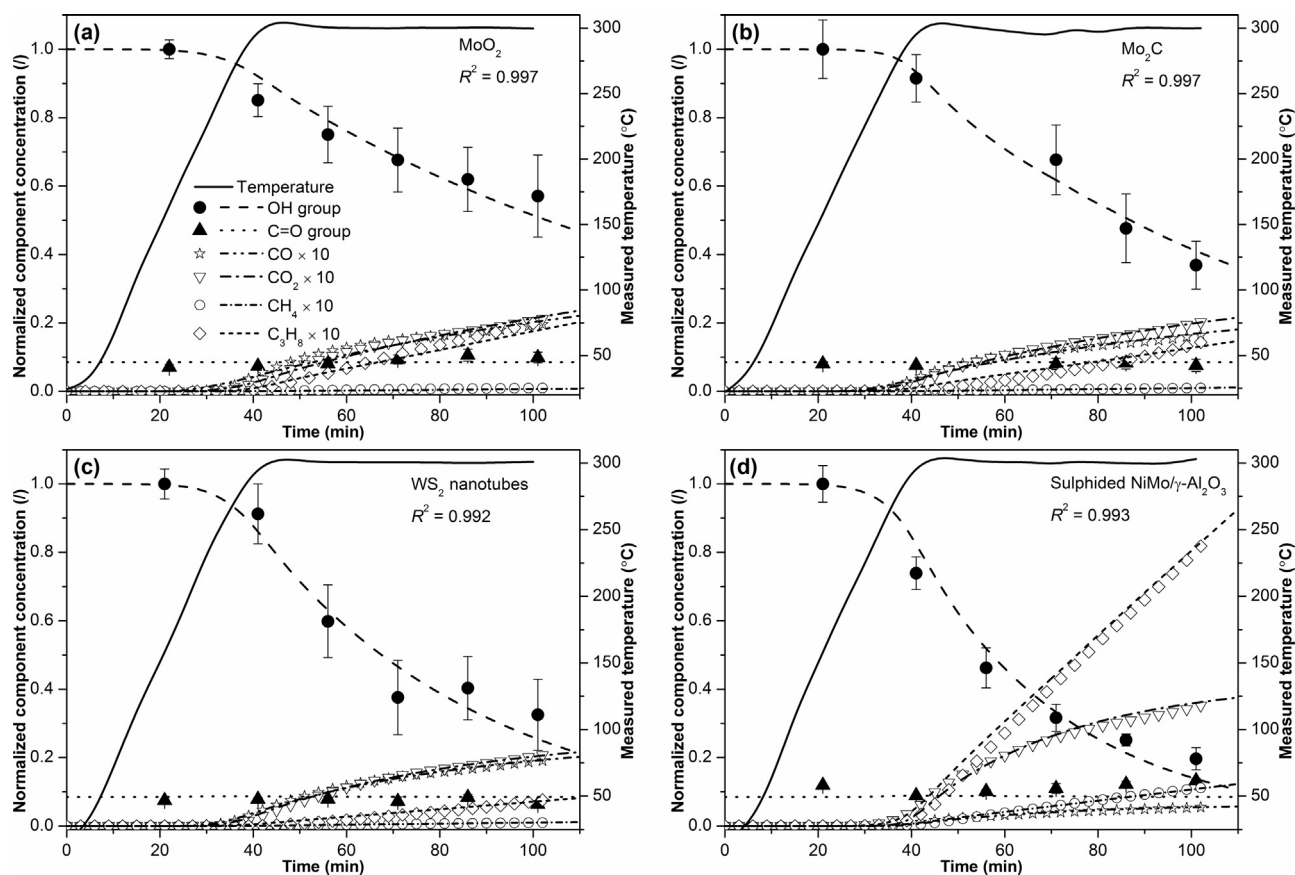


**Fig. 10.** Experimental (symbols) and modelling (lines) results of hydrotreatment using unsupported  $\text{MoO}_2$ ,  $\text{Mo}_2\text{C}$  and  $\text{WS}_2$ , as well as sulphided  $\text{NiMo}/\gamma\text{-Al}_2\text{O}_3$  catalysts; all experiments were performed at the same conditions: temperature of  $300^\circ\text{C}$ , heat-up rate of  $7.5\text{ K min}^{-1}$ , total pressure of  $8\text{ MPa}$ , stirring speed of  $1000\text{ min}^{-1}$ ,  $25\text{ wt}\%$  of tetralin per mass of liquid phase, and  $1.5\text{ wt}\%$  of catalyst per mass of liquefied biomass (except for  $\text{NiMo}/\gamma\text{-Al}_2\text{O}_3$  run, where catalyst content was  $7.5\text{ wt}\%$ , since actual  $\text{MoS}_2$  content was proportionally lower); values of normalized gas concentrations ( $\text{CO}_2$ ,  $\text{CO}$ ,  $\text{CH}_4$  and  $\text{C}_3\text{H}_8$ ) have been multiplied by the factor of 10 to grant better clarity in given scale; legend refers to all subfigures.

values can be compared to evaluate the catalytic activity of the material for joint  $\text{CO}$  and  $\text{CO}_2$  formation, and consequently, for the calculation of the selectivity of (hydroxyl group) hydrodeoxygenation ( $S_{\text{HDO}} = k_1/(k_1 + k_2)$ ), while the ratio  $k_4/k_3$  provides an information regarding the selectivity towards either decarboxylation (a high  $k_4/k_3$  ratio) or decarbonylation (a low  $k_4/k_3$  ratio). The absence of catalyst resulted in the lowest calculated reaction rate constant for reactive carbonyl precursor formation among all runs ( $k_2$  being  $(7.9 \pm 0.4) \times 10^{-4}\text{ min}^{-1}$ ) that is 45% lower in comparison to the run with urchin-like  $\text{MoS}_2$ , where the highest dehydrogenation rate constant was calculated. The ratio  $k_4/k_3$  for the experiment with urchin-like  $\text{MoS}_2$  ( $1.1 \pm 0.1$ ) predicts a nearly equimolar formation of  $\text{CO}$  and  $\text{CO}_2$ , while a slightly higher selectivity towards decarboxylation is expected for blank run (the  $k_4/k_3$  ratio of  $1.4 \pm 0.1$ ). Fig. 9b and d confirms the evaluation of selectivity based on the  $k_4/k_3$  ratio, while the effect of the differing  $k_2$  is not that obvious, since hydroxyl group concentration is significantly lower during the reaction in the presence of urchin-like  $\text{MoS}_2$ , and therefore, gas formation is similar for catalysed and blank run despite different reaction rate constants.

The highest selectivity towards decarboxylation using the unsupported catalyst was observed with  $\text{MoS}_2(\text{IF})/\text{C}$  material (the  $k_4/k_3$  ratio of  $1.8 \pm 0.1$ ), presumably as an artefact of the interconnected carbon in catalyst sample; however the selectivity of alumina-supported  $\text{NiMo}$  catalysts is even higher (the  $k_4/k_3$  ratio of  $7 \pm 2$ ). Despite the noticeable differences in the rate constants  $k_2$ , the latter being the rate-determining step for  $\text{CO}$  and  $\text{CO}_2$  formation, as well as the  $k_4/k_3$  ratios that influenced the selectivity

of decarbonylation and decarboxylation, it can be concluded that the extent of decarbonylation or decarboxylation, observed in this study, is generally minor. Decarbonylation or decarboxylation mostly result from the thermal processes in bulk liquid phase and are only insignificantly catalysed by  $\text{MoS}_2$  or other unsupported materials used in this study, since  $\text{CO}/\text{CO}_2$  yields were very close to those of a blank run.

In comparison to the commercially available (hydrotreatment) catalysts on acidic support [27], cracking and hydrocracking reactions generally remained slow for the unsupported catalysts. A slight cracking activity was nonetheless detected upon utilizing  $\text{MoO}_2$  catalysts ( $k_6$  being the highest), which is also reflected in a low viscosity of liquid product that enabled the successful phase separation by centrifugation (Fig. 7). Non-polar phase yield was surprisingly high by using  $\text{MoO}_2$ , although its oxygen content and tar residue were still considerably higher in comparison to the experiments with  $\text{MoS}_2$  catalysts, as a result of a significantly lower HDO rate (embodied in  $k_1$ ) that can be observed in Figs. 9 and 10 through a lower OH group conversion at the termination of hydrotreatment.

Hydroxyl groups are significantly more vulnerable for HDO than carbonyl groups, since majority of carbonyl groups present in the solvolysis oil are not accessible for decarbonylation or decarboxylation (Fig. 1), while the hydrogenation of the present carbonyl moieties to hydroxyl group is obviously not dominant. The observed rate of  $\text{C}-\text{OH}$  group removal is higher than a relatively resistant  $\text{C}=\text{O}$ , which is in good correlation with HDO computational modelling results, reported by Dupont *et al.* [36]. The authors determined the adsorption energies of the model

**Table 2**  
Calculated apparent rate constants for liquefied biomass deoxygenation at 300 °C.

Catalyst	$k_1$ (min <sup>-1</sup> )	$k_2$ (min <sup>-1</sup> )	$k_3$ (min <sup>-1</sup> ) <sup>a</sup>	$k_4$ (min <sup>-1</sup> ) <sup>a</sup>	$k_4/k_3$	$k_5$ (min <sup>-1</sup> ) <sup>b</sup>	$k_6$ (min <sup>-1</sup> ) <sup>c</sup>
Urchin-like MoS <sub>2</sub>	$4.2 \pm 0.2 \times 10^{-2}$	$1.45 \pm 0.01 \times 10^{-3}$	$7.14 \times 10^{-2}$	$7.71 \times 10^{-2}$	$1.1 \pm 0.1$	$1.54 \pm 0.02 \times 10^{-5}$	$1.47 \pm 0.05 \times 10^{-4}$
MoS <sub>2</sub> (IF)/C	$2.30 \pm 0.03 \times 10^{-2}$	$1.19 \pm 0.05 \times 10^{-3}$	$7.64 \times 10^{-2}$	$1.38 \times 10^{-1}$	$1.8 \pm 0.1$	$2.69 \pm 0.02 \times 10^{-5}$	$2.4 \pm 0.1 \times 10^{-4}$
Commercial MoS <sub>2</sub>	$1.43 \pm 0.02 \times 10^{-2}$	$1.11 \pm 0.04 \times 10^{-3}$	$2.09 \times 10^{-1}$	$2.73 \times 10^{-1}$	$1.3 \pm 0.1$	$1.87 \pm 0.02 \times 10^{-5}$	$1.8 \pm 0.1 \times 10^{-4}$
MoO <sub>2</sub>	$7.8 \pm 0.2 \times 10^{-3}$	$8.15 \pm 0.33 \times 10^{-4}$	$3.04 \times 10^{-1}$	$3.62 \times 10^{-1}$	$1.2 \pm 0.1$	$1.54 \pm 0.04 \times 10^{-5}$	$3.14 \pm 0.02 \times 10^{-4}$
Mo <sub>2</sub> C	$1.21 \pm 0.02 \times 10^{-2}$	$8.56 \pm 0.43 \times 10^{-4}$	$3.09 \times 10^{-1}$	$3.98 \times 10^{-1}$	$1.3 \pm 0.1$	$1.57 \pm 0.02 \times 10^{-5}$	$2.0 \pm 0.1 \times 10^{-4}$
WS <sub>2</sub> nanotubes	$1.76 \pm 0.04 \times 10^{-2}$	$1.02 \pm 0.07 \times 10^{-3}$	$2.23 \times 10^{-1}$	$2.58 \times 10^{-1}$	$1.2 \pm 0.1$	$1.54 \pm 0.02 \times 10^{-5}$	$1.10 \pm 0.04 \times 10^{-4}$
No catalyst	$1.09 \pm 0.02 \times 10^{-2}$	$7.9 \pm 0.4 \times 10^{-4}$	$3.39 \times 10^{-1}$	$4.71 \times 10^{-1}$	$1.4 \pm 0.1$	$1.97 \pm 0.03 \times 10^{-5}$	$1.92 \pm 0.06 \times 10^{-4}$
Industrial sulphided NiMo/γ-Al <sub>2</sub> O <sub>3</sub> [27]	$2.67 \pm 0.05 \times 10^{-2}$	$9.5 \pm 0.6 \times 10^{-4}$	$4.24 \times 10^{-2}$	$3.04 \times 10^{-1}$	$7 \pm 2$	$1.12 \pm 0.01 \times 10^{-4}$	$8.65 \pm 0.08 \times 10^{-4}$

<sup>a</sup> Dehydrogenation ( $k_2$ ) is the rate-determining step for CO and CO<sub>2</sub> formation, since the rate constants for decarbonylation and decarboxylation ( $k_3$  and  $k_4$ ) are an order of magnitude higher, hence their values could not be precisely calculated; however, their ratio ( $k_4/k_3$ ) is an important factor that controls CO<sub>2</sub>/CO selectivity.

<sup>b</sup> Actual unit of rate constant is mol<sub>CH<sub>4</sub></sub> mol<sub>OH</sub><sup>-1</sup> min<sup>-1</sup>.

<sup>c</sup> Actual unit of rate constant is mol<sub>CH<sub>3</sub>OH</sub> mol<sub>OH</sub><sup>-1</sup> min<sup>-1</sup>.

oxygen-containing compounds on MoS<sub>2</sub> and NiMoS<sub>2</sub> catalysts; according to their results, the adsorption with the formation of the interaction between Mo and C–OH has the energy advantage between 8.7 and 43.3 kJ mol<sup>-1</sup> compared to the bonding of Mo and C=O. Although this model is not expected to be completely accurate in describing real solvolytic oil hydrotreatment, it may back the underlying reason for a higher MoS<sub>2</sub> catalytic activity towards the removal of hydroxyl group as opposed to carbonyl.

#### 3.4. Structure–activity correlation for unsupported MoS<sub>2</sub>

A similar selectivity for deoxygenation and cracking reactions, the oxygen content in liquid hydrotreated products and their physical appearance was observed by using all MoS<sub>2</sub> samples, while the main difference was in the yield of organic and tar phases, as well as the different reaction kinetics of hydroxyl group removal; hence, variable reaction time is required for reaching the same hydroxyl group conversion.

The use of the prepared MoS<sub>2</sub>(IF)/C and urchin-like MoS<sub>2</sub> materials resulted in a similar oxygen content in organic phase and its yield; however, the yield of semi-solid tar is more than two times higher in the case of composite catalyst (Fig. 7), which could have resulted from the carbon presence in the catalyst, causing the polymeric by-products formation during a run. It was suggested that inorganic fullerenes should have an enhanced catalytic activity due to the presence of the strains in structure [26]. Strained areas could probably have a lower energy of Mo–S bonding, which allows the formation of active sites. A lower HDO rate on MoS<sub>2</sub>(IF)/C sample compared to urchin-like material, alongside with a similar composition of the products under equal reaction conditions, might indicate that MoS<sub>2</sub>(IF)/C possess a lower amount of active sites. The activity of carbon-free IF might be higher, since the tested sample contains ~20 wt% of carbon and therefore, the actual amount of MoS<sub>2</sub> is proportionally lower. The carbon deposition over active phase is also expected to physically block the latter, as can be observed from the TEM image (Fig. 5), hence creating the barrier towards reactive compound–catalyst interaction. Moreover, MoS<sub>2</sub>(IF)/C material has a low pore size (19.3 Å) compared to other samples (Table 1), therefore the internal transport resistance towards the penetration of the depolymerised cellulose or lignin molecules to the active sites of IF, located inside a relatively large agglomerate, might significantly influence the global reaction rate.

An increased activity of urchin-like MoS<sub>2</sub> is presumably caused by a high concentration of active sites, while the morphology of radial crystalline needles growing from the same centre is expected to be beneficial, since this morphology should decrease the internal mass-transfer limitation of the reactants to active sites [25]. Urchin-like morphology is also advantageous over the traditional porous materials in terms of preventing physical deactivation, since active sites are located on exposed nano-needles and not inside tubular pores that are vulnerable to plugging, which is especially important when hydro-processing real biomass-derived oils.

#### 4. Conclusions

This work provides a novel insight into the biomass-derived oils' hydrodeoxygenation over unsupported MoS<sub>2</sub>, WS<sub>2</sub>, MoO<sub>2</sub> and Mo<sub>2</sub>C catalysts with the emphasis on the influence of different morphology of MoS<sub>2</sub> materials. The synthesis and characterisation of novel composite MoS<sub>2</sub>(IF)/C material and urchin-like MoS<sub>2</sub> was reported. MoS<sub>2</sub>(IF)/C represents the first example of composite, containing MoS<sub>2</sub> inorganic fullerenes interconnected with carbon, that was prepared in a single step. Inorganic fullerene units with ~12 nm size are interconnected by amorphous carbon inclusions and form the agglomerates with 50–100 μm size. Molybdenum

showed the highest activity and selectivity towards HDO in its sulphide form, since up to three times higher hydroxyl group removal rate was observed by measurement and modelling study when using the prepared urchin-like  $\text{MoS}_2$  or  $\text{MoS}_2(\text{IF})/\text{C}$  in comparison to the commercially available  $\text{MoS}_2$  sample. Moreover, the oil phase yields with the oxygen content of 8.5 wt% and the gross calorific value of  $38 \text{ MJ kg}^{-1}$  were also very high by using the prepared materials, while the use of  $\text{WS}_2$ ,  $\text{Mo}_2\text{C}$  and  $\text{MoO}_2$  reflected in either low HDO activity or the undesired rheological properties of liquid product. When paralleled to the commercially available  $\text{NiMo}/\gamma\text{-Al}_2\text{O}_3$  catalyst with a similar  $\text{MoS}_2$  loading, the hydroxyl group removal rate was comparable, while deoxygenation was much more selective towards the hydrogenolysis by using unsupported  $\text{MoS}_2$ . On the other hand, decarbonylation, decarboxylation and hydrocracking were not favoured by the unsupported materials tested in this study as a result of the absence of acid sites that are generally responsible for C–C bond cleavage.

### Acknowledgements

The authors gratefully acknowledge the financial support of the Slovenian Research Agency (ARRS) through the Program P2-0152. The authors also acknowledge Gozdno Gospodarstvo Postojna for oil sample provision and Ms. Eva Kovič for her excellent laboratory work.

### Appendix A. Supplementary data

Supplementary data associated with this article can be found, in the online version, at <http://dx.doi.org/10.1016/j.apcatb.2014.08.032>.

### References

- [1] M. Balat, *Energy Sources A* 28 (2006) 517–525.
- [2] T. Seljak, S. Rodman Oprešnik, M. Kunaver, T. Katrašnik, *Appl. Energy* 99 (2012) 40–49.
- [3] E. Furimsky, *Appl. Catal. A* 199 (2000) 147–190.
- [4] A.V. Bridgwater, *Appl. Catal. A* 116 (1994) 5–47.
- [5] D.C. Elliott, *Energy Fuels* 21 (2007) 1792–1815.
- [6] A.D. Sutton, F.D. Waldie, R. Wu, M. Schlaf, L.A. 'Pete' Silks, J.C. Gordon, *Nat. Chem.* 5 (2013) 428–432.
- [7] L. Vilcoq, R. Koerin, A. Cabiac, C. Espécel, S. Lacombe, D. Duprez, *Appl. Catal. B* 148–149 (2014) 499–508.
- [8] R.N. Olcese, J. Francois, M.M. Bettahar, D. Petitjean, A. Dufour, *Energy Fuels* 27 (2013) 975–984.
- [9] M.V. Bykova, D.Y. Ermakov, V.V. Kaichev, O.A. Bulavchenko, A.A. Saraev, M.Y. Lebedev, V.A. Yakovlev, *Appl. Catal. B* 113–114 (2012) 296–307.
- [10] O.İ. Şenol, E.M. Ryymin, T.R. Viljava, A.O.I. Krause, *J. Mol. Catal. A: Chem.* 268 (2007) 1–8.
- [11] S. Brillouet, E. Baltag, S. Brunet, F. Richard, *Appl. Catal. B* 148–149 (2014) 201–211.
- [12] Z. He, X. Wang, *Catal. Sustain. Energy* 1 (2012) 28–52.
- [13] E. Laurent, B. Delmon, *J. Catal.* 146 (1994) 281–291.
- [14] E. Laurent, B. Delmon, G.F. Froment (Eds.), *Studies in Surface Science and Catalysis*, Elsevier, 1994, pp. 459–466.
- [15] O.İ. Şenol, T.R. Viljava, A.O.I. Krause, *Catal. Today* 106 (2005) 186–189.
- [16] E. Laurent, A. Centeno, B. Delmon, in: B. Delmon, G.F. Froment (Eds.), *Studies in Surface Science and Catalysis*, Elsevier, 1994, pp. 573–578.
- [17] M. Ruinart de Brimont, C. Dupont, A. Daudin, C. Geantet, P. Raybaud, *J. Catal.* 286 (2012) 153–164.
- [18] Y.Q. Yang, C.T. Tye, K.J. Smith, *Catal. Commun.* 9 (2008) 1364–1368.
- [19] P. Afanasiev, *J. Catal.* 269 (2010) 269–280.
- [20] Y. Okamoto, K. Hioka, K. Arakawa, T. Fujikawa, T. Ebihara, T. Kubota, *J. Catal.* 268 (2009) 49–59.
- [21] Y. Okamoto, A. Kato, N. Usman, T. Rinaldi, H. Fujikawa, I. Koshika, T. Hiromitsu, J. Kubota, *Catalysis* 265 (2009) 216–228.
- [22] Z. Li, J. Liu, H. Wang, E. Wang, B. Wang, X. Ma, S. Qin, Q. Sun, *J. Mol. Catal. A: Chem.* 378 (2013) 99–108.
- [23] B. Yoosuk, D. Tumnantong, P. Prasassarakich, *Fuel* 91 (2012) 246–252.
- [24] B. Yoosuk, D. Tumnantong, P. Prasassarakich, *Chem. Eng. Sci.* 79 (2012) 1–7.
- [25] G. Veryasov, M. Grilc, B. Likozar, A. Jesih, *Catal. Commun.* 46 (2014) 183–186.
- [26] J.A. Ascencio, M. Perez-Alvarez, L.M. Molina, P. Santiago, M. José-Yacaman, *Surf. Sci.* 526 (2003) 243–247.
- [27] M. Grilc, B. Likozar, J. Levec, *Appl. Catal. B* 150–151 (2014) 275–287.
- [28] M. Kunaver, E. Jasiukaitytė, N. Čuk, *Bioresour. Technol.* 103 (2012) 360–366.
- [29] M. Grilc, B. Likozar, J. Levec, *Biomass Bioenergy* 63 (2014) 300–312.
- [30] G. Alonso, G. Berhault, F. Paraguay, E. Rivera, S. Fuentes, R.R. Chianelli, *Mater. Res. Bull.* 38 (2003) 1045–1055.
- [31] L.K. Herrera, A. Justo, A. Muñoz-Páez, J.A. Sans, G. Martínez-Criado, *Anal. Bioanal. Chem.* 395 (2009) 1969–1975.
- [32] G.L. Frey, R. Tenne, M.J. Matthews, M.S. Dresselhaus, G. Dresselhaus, *Phys. Rev. B* 60 (1999) 2883–2892.
- [33] C.T. Tye, K.J. Smith, *Catal. Today* 116 (2006) 461–468.
- [34] R. Poli, *Coord. Chem. Rev.* 252 (2008) 1592–1612.
- [35] N. Li, G.W. Huber, *J. Catal.* 270 (2010) 48–59.
- [36] C. Dupont, R. Lemeur, A. Daudin, P. Raybaud, *J. Catal.* 279 (2011) 276–286.